

Coherent phonon generation in laser-heated gold nanofilm

Cite as: J. Chem. Phys. **152**, 124704 (2020); <https://doi.org/10.1063/1.5137818>

Submitted: 13 November 2019 . Accepted: 05 March 2020 . Published Online: 23 March 2020

Xuan Wang, Junjie Li, and Jianming Cao 

COLLECTIONS

Paper published as part of the special topic on [Ultrafast molecular sciences by femtosecond photons and electrons](#)

Note: This paper is part of the JCP Special Topic on Ultrafast Molecular Sciences by Femtosecond Photons and Electrons.



View Online



Export Citation



CrossMark

ARTICLES YOU MAY BE INTERESTED IN

[Potential energy shift of the Fermi level at plasmonic structures for light-energy conversion determined by graphene-based Raman measurements](#)

The Journal of Chemical Physics **152**, 124702 (2020); <https://doi.org/10.1063/1.5143560>

[Can second order nonlinear spectroscopies selectively probe optically “dark” surface states in small semiconductor nanocrystals?](#)

The Journal of Chemical Physics **152**, 120901 (2020); <https://doi.org/10.1063/1.5139208>

[ABINIT: Overview and focus on selected capabilities](#)

The Journal of Chemical Physics **152**, 124102 (2020); <https://doi.org/10.1063/1.5144261>

Lock-in Amplifiers
up to 600 MHz



Coherent phonon generation in laser-heated gold nanofilm

Cite as: J. Chem. Phys. 152, 124704 (2020); doi: 10.1063/1.5137818

Submitted: 13 November 2019 • Accepted: 5 March 2020 •

Published Online: 23 March 2020



View Online



Export Citation



CrossMark

Xuan Wang,^{1,a)} Junjie Li,² and Jianming Cao^{3,4,a)} 

AFFILIATIONS

¹Beijing National Laboratory for Condensed Matter Physics, Institute of Physics, Chinese Academy of Sciences, Beijing 100190, China

²Condensed Matter Physics and Material Science Department, Brookhaven National Laboratory, Upton, New York 11973-5000, USA

³Physics Department and National High Magnetic Field Laboratory, Florida State University, Tallahassee, Florida 32310, USA

⁴Center for Ultrafast Science and Technology, Key Laboratory for Laser Plasmas (Ministry of Education), School of Physics and Astronomy, Collaborative Innovation Center of IFSA (CICIFSA), Shanghai Jiao Tong University, Shanghai 200240, China

Note: This paper is part of the JCP Special Topic on Ultrafast Molecular Sciences by Femtosecond Photons and Electrons.

a) Authors to whom correspondence should be addressed: xw@iphy.ac.cn and jcao@magnet.fsu.edu

ABSTRACT

We have studied the mechanism of coherent acoustic phonon generation in gold nanofilm induced by ultrafast laser-heating. Under the non-equilibrium condition when the lattice heating time is much longer than the film vibration period, we clearly identified the contribution of electronic thermal stress to drive the lattice motion and successfully measured the electronic Grüneisen parameter γ^e to be 1.6 ± 0.3 . We also found that lattice heating via the electron–phonon coupling process lagged behind the coherent lattice motion, which we attributed to the prolonged thermalization process of the laser-excited non-thermal electrons under high pumping conditions. By taking such a process into account, the improved model fit our experimental data much better, and the extracted γ^e of gold was still around 1.6.

Published under license by AIP Publishing. <https://doi.org/10.1063/1.5137818>

I. INTRODUCTION

Photo-induced coherent acoustic phonons have been extensively studied in various crystals by using time-resolved techniques based on ultrafast lasers.¹ They are closely related to the energy transfer between the excited electrons and lattice (lattice heating) and the instantaneous change in the electronic energy distribution that modifies the interatomic forces. Particularly, when a noble metal such as gold is irradiated, the energy transfer takes place in multiple steps. Initially, only electrons absorb photons and are excited to higher energy states. Then, these electrons (called non-thermal electrons) very quickly redistribute their energy by electron–electron coupling and tend to build a new thermal equilibrium only within the electron subsystem,^{2–4} which is called electron thermalization. Meanwhile, they relax their excess energy to the lattice by relatively slow electron–phonon coupling,^{3,5} and this coupling is greatly enhanced after electron thermalization. In about

10 ps, a final thermal equilibrium between the electron and lattice (lattice thermalization) is established. During such a heating process, coherent lattice motion is also launched such that the lattice starts to expand and oscillate.¹ It can be viewed as a superposition of various acoustic phonon modes, whose generation mechanism is usually described using photo-induced thermal stress that converts optical energy into mechanical energy. For a nonmagnetic metal such as gold, the thermal stress (σ) consists of two independent contributions: the thermal stress related to the lattice anharmonicity (also called thermoelastic effect) and the pressure from excited electrons related to the deformation potential. They are characterized by the Grüneisen parameter (γ) and the energy change of each subsystem (ΔE),⁶

$$\sigma = \gamma^e \Delta E^e + \gamma^l \Delta E^l, \quad (1)$$

where the superscripts e and l represent the electron and lattice subsystem, respectively. Later in this article, we would call them

electronic and lattice thermal stress, respectively, although, to be more accurate, both stresses are related to the energy distribution of electrons. The non-equilibrium condition created by ultrafast laser-heating significantly enhances the electronic contribution towards launching the coherent phonons as the excess energy is initially stored in the electron subsystem. By using such a scheme, the mechanism of coherent acoustic phonon generation, especially the contribution from the electronic thermal stress, has been studied by all-optical pump-probe methods,^{7–9} ultrafast electron diffraction (UED),^{10,11} and ultrafast x-ray diffraction (UXD).¹² Here, UED and UXD have unique advantages—they can monitor both lattice heating and lattice coherent motion simultaneously, and therefore reveal the correlation between these two aspects of lattice dynamics in detail. By using UED, we have investigated the role of the electronic thermal stress in driving the coherent acoustic phonons in aluminum and nickel thin films^{10,11} and developed a new methodology to measure γ^e , a task that with conventional measurement was only possible at very low temperatures.^{13,14} We found that a key factor for such a measurement under the laser-induced non-equilibrium condition is the reduction in the ratio (α) of lattice thermalization time ($3\tau_{e-p}^E$) over the quarter period ($\Gamma/4$) of coherent lattice vibration, $\alpha = 12\tau_{e-p}^E/\Gamma$, so that the lattice can respond fast enough to the initial transient electronic thermal stress.¹⁵ In the case of aluminum and nickel, τ_{e-p}^E is only about 0.7 ps. Even in a film as thin as 20 nm, the vibration period is around 10 ps making α smaller than 1. Therefore, it requires a high signal-to-noise ratio (SNR) and long data acquisition time to observe the effect of the electronic thermal stress on the lattice coherent motion.

In this paper, we applied the same method to a gold thin film, whose τ_{e-p}^E and Γ were both around 4 ps, making α bigger than 10. Under such conditions, the effect of the electronic thermal stress on acoustic phonon generation is more pronounced. The γ^e of gold was determined to be around 1.6, consistent with previous studies.^{12,16} We also observed that the electron-phonon coupling process started 1 ps later than the thermal expansion, which could be attributed to the slowdown of the electron thermalization process under high pumping conditions. By taking such a process into account, the γ^e of gold was still around 1.6, while the quality of the model-fitting is greatly improved.

II. EXPERIMENT

The experiments were conducted on the second-generation ultrafast electron diffraction instrument with an increased electron-beam energy of 85 kV.¹⁷ A typical pump-probe measurement is utilized to monitor the ultrafast structural dynamics of the sample. In such an experiment, the 1 mJ laser output pulses centered at the 800 nm wavelength with a repetition rate of 1 kHz were split using a beam splitter (BS), resulting in a pump beam and a probe beam with 90% and 10% of the initial laser beam energy, respectively. The pump beam was first sent to a linear motion stage, which was used to control the time delay between the pump and probe beams, and then focused onto the sample to initiate sample heating. The probe beam was frequency tripled to provide sufficient photon energy to eject electrons from the photo-cathode inside the electron gun. The electron diffraction patterns (DPs) were intensified and recorded

by using a cooled CCD camera. The experiments were performed under ultra-high vacuum (UHV) conditions with a base pressure of 4×10^{-10} torr. To obtain enough SNR, we used a larger number of electrons per pulse than previous experiments.^{10,11} Due to the geometrical mismatch¹⁸ between the pump and probe beams and the pulse-width of the electron beam, the overall temporal resolution of the experiment was about 800 fs.

The sample was a gold thin film on a silicon dioxide substrate. First, about 8 nm Au thin film was evaporated on a freshly cleaved salt substrate. Immediately after the evaporation, SiO₂ was sputtered on the top to form a 20 nm supporting film. The salt substrate was dissolved in distilled water leaving the Au/SiO₂ film floating on the water surface. The film was then carefully picked up onto a TEM grid and subsequently mounted onto a customized UHV compatible sample holder.

To obtain a quantitative measurement of structural changes, the recorded two-dimensional DPs were converted to a 1D intensity radial profile, as shown in Fig. 2(c). After subtracting the diffused scattering background, each Bragg peak of Au in the intensity curve was fitted with a Gaussian line profile to determine its peak center (peak position), peak intensity, and peak width. The diffraction peak intensity can be related to the lattice temperature T through the Debye-Waller factor (DWF),¹⁹

$$I_{(h,k,l)}(T) \propto I_{(h,k,l)}(T_0) \exp\left(\frac{-(B(T) - B(T_0))(h^2 + l^2 + k^2)}{2a^2}\right), \quad (2)$$

where a is the lattice constant. $I_{(h,k,l)}(T)$ represents the overall intensity of the diffraction peak specified by Miller indices: h , k , and l . $B(T)$ is the Debye-Waller factor that, to the first order approximation, increases linearly with T .¹⁹ Using the peak intensity before the laser excitation [$I_{(h,k,l)}(T_0)$] as a reference and according to Eq. (2), we have

$$\Delta T \propto -\ln \frac{I_{(h,k,l)}(T)}{I_{(h,k,l)}(T_0)}, \quad (3)$$

where the temperature jump $\Delta T = T - T_0$. Equation (3) links the change in the diffraction peak intensity to that in the lattice temperature. Meanwhile, the diffraction peak position change is related to lattice constant change by Bragg's law, $2d_{(h,k,l)}\sin(\theta) = \lambda$, where $d_{(h,k,l)}$ is the interplanar distance of the (h, k, l) lattice planes. θ is half of the diffraction angle, and λ is the de Broglie wavelength of the 85 keV probing electrons. For small diffraction angles, the relative peak position change can be related to the lattice constant change by the following equation:

$$\frac{\Delta\theta}{\theta} = -\frac{\Delta d_{(h,k,l)}}{d_{(h,k,l)}}. \quad (4)$$

Hence, UED enables us to monitor both the lattice coherent motion and the thermal motion (through lattice temperature) simultaneously, providing a more complete picture of the transient lattice dynamics in the sub-ps time scale.

In the transmission geometry as shown in Fig. 1, the diffraction peak position is only sensitive to the vibration and lattice parameter changes projected on the transverse direction (perpendicular to the trajectory of the electrons). However, we believe that our nm-thick film sample is not perfectly flat but has many

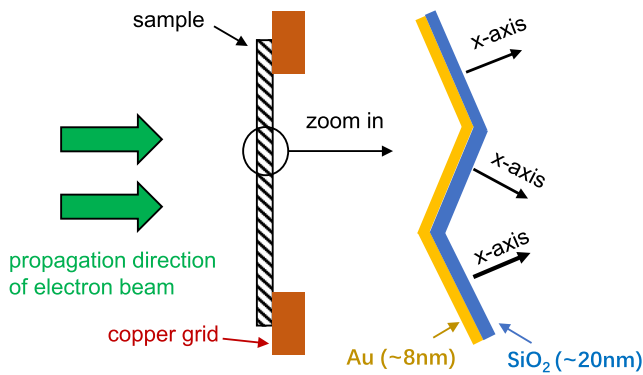


FIG. 1. The transmission geometry of electron diffraction. The electron probe propagates perpendicular to the sample macroscopically. However, the nm-thick film sample is not perfectly flat but has many wrinkles across the probed region such that the vibration along the film normal (defined as x-axis) in each wrinkle can be observed.

wrinkles across the probed region such that the projection of the normal vibration (along the x-axis) on the transverse direction can be observed.

III. RESULT AND DISCUSSION

The temporal evolutions of the peak intensity and peak position are shown in Fig. 2. According to Eq. (3), the peak intensity is plotted

in a way proportional to the lattice temperature of Au. The increase in lattice temperature reflects the thermalization between electrons and the lattice (or lattice heating). Such a process is usually explained by the so-called two temperature model (TTM)²⁰ or its advanced version,²¹ which fits the temporal evolution of both hot electron and lattice temperatures (T^e and T^l , respectively) simultaneously. However, under our experimental condition, we found that the simulated curve of T^l based on TTM only slightly deviated from an exponential function, which had negligible effect on finding γ^e later. Hence, the change in lattice temperature of Au (ΔT_1^l) was simply modeled by

$$\Delta T_1^l = \begin{cases} 0, & 0 \leq t \leq t_0 \\ T_{jump} (1 - \exp(-\frac{t-t_0}{\tau_{e-p}^E})), & t_0 < t \end{cases} \quad (5)$$

where T_{jump} is the overall lattice temperature jump of Au induced by laser-heating. t_0 is the time-zero, which is floated in the fitting. τ_{e-p}^E is the coupling time-constant between the electron and the lattice from the energy point of view. Fitting our data by Eq. (5) gave $\tau_{e-p}^E = 4.4$ ps, consistent with previous studies.^{12,22} Also in this model, the thermalization process of electrons was assumed to be instantaneous. Compared with the peak position data, the t_0 of the intensity fitting curve delayed about 1.2 ps, marked as Δt_0 in Fig. 2(a). We attributed this to the effect that electron-phonon coupling becomes significant only after electron thermalization, which will be elaborated in detail later. Similar to aluminum and nickel thin films,^{10,11} the lattice motion in the Au film also showed some vibrations, although its amplitude was much smaller.

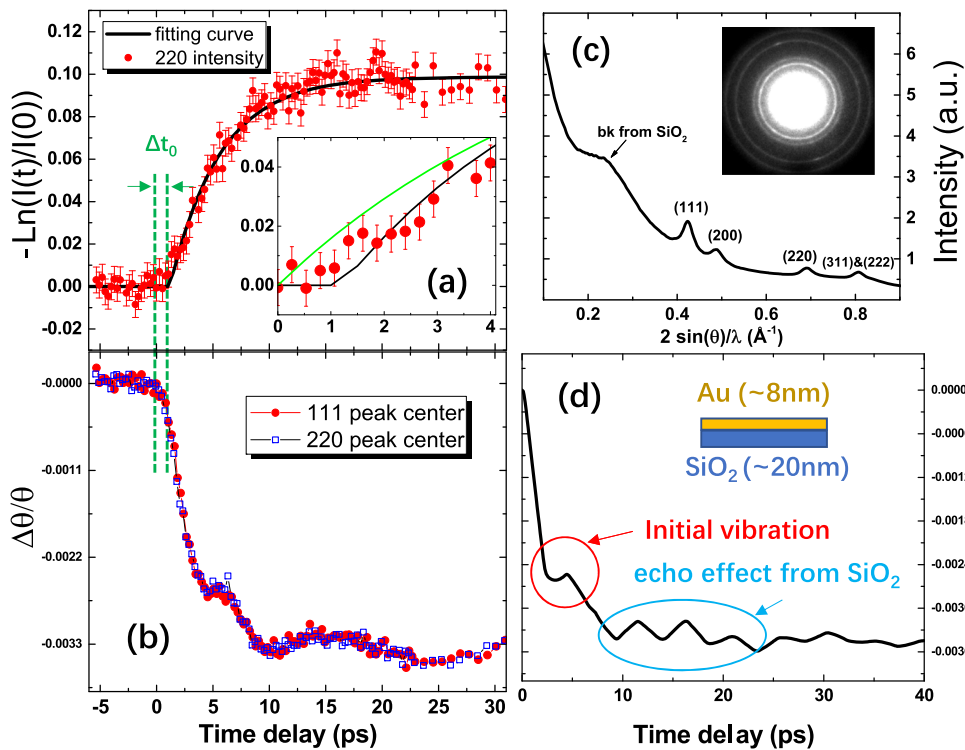


FIG. 2. (a) 220 peak intensity as a function of delay time. The black line is the fitting by an exponential function with a floating time-zero. The inset highlights the first 4 ps of the curve. The green line is the initial part of the co-time-zero-intensity fitting, which links its time-zero to that of the peak position data. Co-time-zero-intensity fitting shifts the time-zero of the black curve to the left by Δt_0 . The full curve of such fitting is shown in the inset of Fig. 3(a). (b) 111 and 220 peak positions as a function of delay time. (c) A typical 2D diffraction pattern of Au captured by UED and its corresponding 1D intensity profile. (d) The simulation of the coherent lattice motion in Au that resembles our experimental data.

To understand the mechanism of such coherent phonon generation, we considered the Au/SiO₂ film as a continuous elastic medium, consisting of many wrinkles as shown in Fig. 1. The transverse scale of such wrinkles is still much bigger than the sample's thickness so that the thermal expansion along the in-plane direction can be ignored in the time scale of 10 ps.²³ On the other hand, the 1D breathing motion along the film normal direction can be described as^{1,23}

$$\frac{\partial^2 u_1(x, t)}{\partial t^2} = v_1^2 \frac{\partial^2 u_1(x, t)}{\partial x^2} - 2\beta_1 \frac{\partial u_1(x, t)}{\partial t} - \frac{1}{\rho_1} \frac{\partial \sigma_1(x, t)}{\partial x}, \quad 0 \ll x \ll l_1, \quad (6)$$

$$\frac{\partial u_1(x, t)}{\partial x} \Big|_{x=0} = 0, \quad (7)$$

$$\frac{\partial^2 u_2(x, t)}{\partial t^2} = v_2^2 \frac{\partial^2 u_2(x, t)}{\partial x^2} - 2\beta_2 \frac{\partial u_2(x, t)}{\partial t} - \frac{1}{\rho_2} \frac{\partial \sigma_2(x, t)}{\partial x}, \quad l_1 \ll x \ll l_2, \quad (8)$$

$$\frac{\partial u_2(x, t)}{\partial x} \Big|_{x=l_2} = 0, \quad (9)$$

$$\rho_1 v_1^2 \frac{\partial u_1(x, t)}{\partial x} \Big|_{x=l_1} = \rho_2 v_2^2 \frac{\partial u_2(x, t)}{\partial x} \Big|_{x=l_1} + \sigma_1(l_1, t), \quad (10)$$

$$u_1(l_1, t) = u_2(l_1, t), \quad (11)$$

where the positive direction of the x-axis is set along the film normal for each wrinkle, pointing from Au to SiO₂. $u(x, t)$, v , β , and ρ represent the lattice displacement along the x-axis, lattice sound speed, damping constant, and density, respectively. The subscript 1 and 2 stand for Au and SiO₂, respectively. l_1 and l_2 are Au and Au/SiO₂ film thickness, respectively. The initial and boundary conditions are

$$u_{1,2}(x, 0) = 0, \quad (12)$$

$$\frac{\partial u_{1,2}(x, t)}{\partial t} \Big|_{t=0} = 0. \quad (13)$$

Given that the combination of the penetration depth of the 800 nm laser and the initial ballistic transport range of the excited electrons in Au well exceed the sample thickness,²⁴ the Au film can be considered heated-up homogeneously. Meanwhile, SiO₂ did not absorb the laser energy. Also considering that the hot electrons are confined in the Au by the barrier formed at the Au/SiO₂ interface and the interfacial heat conduction due to phonon transport is insignificant on the 10 ps time scale, no heating of the SiO₂ film is expected. This is consistent with the observed peak intensity curve of gold, which showed no decay induced by any heat transport from Au to SiO₂ in the time scale of 100 ps. Hence, according to Eq. (1), the thermal stress can be written as

$$\sigma_1(x, t) = \gamma_1^e \Delta E_1^e(t) + \gamma_1^l \Delta E_1^l(t), \quad (14)$$

$$\sigma_2(x, t) = 0, \quad (15)$$

where both ΔE^l and ΔE^e are energy changes with reference to their values before time-zero. After the thermalization of electrons, the total energy among hot electrons and lattice is conserved,

$$\frac{\partial \Delta E_1^e(t)}{\partial t} = -\frac{\partial \Delta E_1^l(t)}{\partial t} \Rightarrow C_1^e \frac{\partial T_1^e(t)}{\partial t} = -C_1^l \frac{\partial T_1^l(t)}{\partial t}, \quad (16)$$

where C_1^e is the electronic heat capacity of Au that increases linearly with electronic temperature $T_1^e(t)$.^{25,26} C_1^l is the lattice heat capacity of Au, which can be considered as a constant because $T_1^l(t)$ is much higher than the lattice Debye temperature (around 150 K–200 K for Au).²⁷ Plugging in Eqs. (5) and (16), Eq. (14) can be written as

$$\sigma_1(x, t) = \begin{cases} 0, & 0 \leq t \leq t_0 \\ C_1^l T_{jump} \gamma_1^l (1 - \zeta \exp(-\frac{t-t_0}{\tau_{e-p}^E})) \\ + \gamma_1^e (E_{laser} - C_1^l T_{jump}), & t_0 \leq t \end{cases}, \quad (17)$$

where

$$\zeta = \frac{\gamma_1^l - \gamma_1^e}{\gamma_1^l} \quad (18)$$

and E_{laser} is the absorbed pumping energy. The last term on the right-hand side of the equation describes the electronic thermal stress after reaching the new thermal equilibrium and was ignored in the simulation because the electronic heat capacity is three orders smaller than that of the lattice in this temperature range.²⁵ Plugging in Eq. (17), Eqs. (6)–(13) were solved numerically. Then, according to Eq. (4), the averaged relative change in peak position can be evaluated by

$$\frac{\Delta \theta}{\theta} = -\frac{\xi}{l_1} \int_0^{l_1} \frac{\partial u(x, t)}{\partial x} dx = -\frac{u(l_1, t) - u(0, t)}{l_1}, \quad (19)$$

where ξ is the projection parameter that characterizes the projection of $u(x, t)$ on the transverse direction detected by electron diffraction and it should be considered as an average of all the wrinkles that contribute to the diffraction peaks. Figure 2(d) shows a typical simulation result in which we used the accepted values $v_1 = 3360$ m s⁻¹, $v_2 = 6000$ m s⁻¹, $\gamma_1^l = 2.96$, and $\gamma_1^e = 1.6$.^{16,28} Both t_0 and τ_{e-p}^E are extracted from the peak intensity fitting curve, as shown in Fig. 2(a). By adjusting other parameters, the simulation result resembled our experimental data to some extent. Particularly, we found that the lattice displacement at the two boundaries, $u(l_1, t)$ and $u(0, t)$, was almost identical in absolute value but with opposite sign in the first 7 ps, similar to a breathing motion of a free-standing film. They were mainly attenuated by the parameters of Au rather than those of SiO₂. At a later time, $u(l_1, t)$ and $u(0, t)$ became different because the acoustic waves once transmitted into SiO₂ film now bounced back and re-entered the Au film (our data implied that the time scale was about 10 ps, roughly the round trip time of the longitudinal sound wave in a 20-nm SiO₂ film). These waves were not in pace with the vibrations in Au, and as a result,

they interfered with one another and generated a beating pattern, which was also seen in the simulation [see the echo effect marked in Fig. 2(d)].

Next, we fitted the peak position data [shown in Fig. 2(b)], particularly for the first 7 ps. First, the amplitude of the thermal stress was adjusted (by T_{jump}) to roughly match the data after 10 ps, where the lattice thermalization was finished and the maximum peak position change could be determined. Then, l_1 , γ_1^e , and β_1 were tuned as free parameters to fit the data of the first 7 ps, and the total variance was used to judge the fitting quality. Finally, l_2 and β_2 were adjusted to match the beating patterns afterward. To highlight the importance of the electronic thermal stress, we first set $\gamma_1^e = 0$ to see if the lattice thermal stress alone could launch such coherent lattice motion. The simulation result is shown in Fig. 3(a). No matter how much we adjust other parameters, the amplitude of the relative peak position change was always smaller than the real data. As mentioned earlier, t_0 obtained from fitting the peak intensity curve delayed about 1.2 ps with reference to that of the peak position data. This together with the finite SNR of experimental data could introduce the discrepancy. To check out this issue, we forced the peak intensity fitting curve to share the same time-zero as that of the peak position data

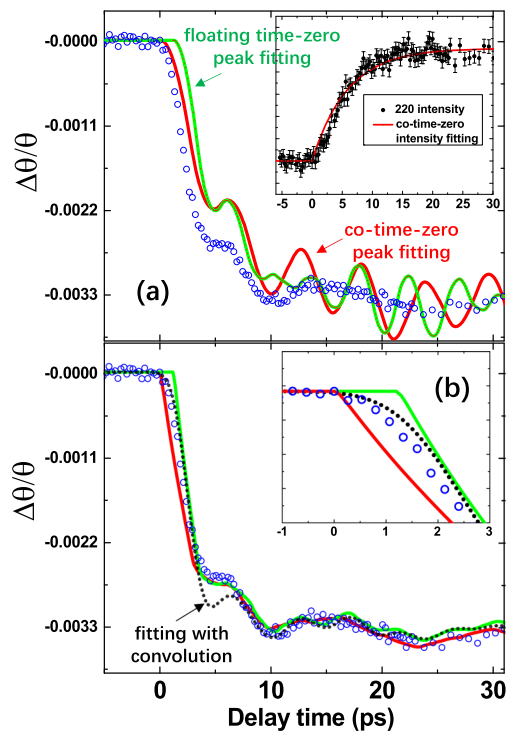


FIG. 3. (a) Fitting the peak position data with $\gamma_1^e = 0$. The blue open circles are experimental data. The green curve is the fitting by using the lattice peak intensity fitting curve with time-zero floated shown in Fig. 2(a), while the red one is by using the curve with time-zero linked to the peak position data (co-time-zero peak fitting shown in the inset of this figure). (b) Fitting the peak position data to find γ_1^e . The green curve and the red curve have the same meanings as in (a). The black-dotted curve is a peak fitting curve, which convolutes a 2 ps Gaussian profile. The inset is the highlight of the initial 3 ps.

[see both the insets of Figs. 2(a) and 3(a)]. Such treatment increased τ_{e-p}^E from 4.4 ps to 5.9 ps, which made the overall peak intensity fitting (co-time-zero intensity fitting) much worse [see both the insets of Figs. 2(a) and 3(a)], and it did not resolve the discrepancy [see the co-time-zero peak fitting in Fig. 3(a)]. Therefore, there must be an extra stress responsible for the earlier stage of lattice motion.

In the next step, we floated γ_1^e and repeated our fitting procedure. As shown in Fig. 3(b), the fitting curve with $\gamma_1^e = 1.6 \pm 0.3$ matched the data very well except for the earlier stage (0–2 ps). We also tried to fit the data by using the co-time-zero intensity fitting scheme and found that the best fitting value of γ_1^e was 1.48 ± 0.3 , although the fitting quality is much worse, as shown in Fig. 3(b). These two values for γ_1^e were both in the range of $\gamma_1^e = 1.6 \pm 0.5$ measured by the conventional method under very low temperature¹⁶ and $\gamma_1^e = 1.48 \pm 0.3$ by using an ultrafast x-ray diffraction technique in the limit of $\alpha \ll 1$.¹² This implied that in the limit of $\alpha \gg 1$, the contribution from the electronic thermal stress became so pronounced that the accuracy in determining γ_1^e depends far less on how accurate in finding t_0 any longer, a key issue of previous studies.

We now focus on the discrepancy between the data and our fitting in the first 1.5 ps, where the peak position change is ahead of the peak intensity fitting curve. First, we ruled out the convolution effect due to finite electron pulse width and geometrical mismatch (about 800 fs). As an example shown in Fig. 3(b), to smooth the sharp turning point, a Gaussian function with a full-width-at-half-maximum (FWHM) as large as 2 ps must be used. However, the peak position fitting curve by this approach failed to match the initial oscillation in the data shown in the first peak around 4 ps in the black-dotted curve because such convolution reduced τ_{e-p}^E from 4.4 ps to 4.0 ps in the peak intensity fitting, which made the lattice reach the new thermal equilibrium much faster. We believed that the discrepancy in the first 1.5 ps originated from the prolonged electron thermalization under high pumping conditions used in the experiment. Such a process takes place in about 1 ps,² close to the time scale of Δt_0 . Within this time range, the electron–phonon coupling is initially very weak and then becomes progressively stronger with time, as the electron thermalization creates a larger number of hot electrons with lower energies, leading to an enhancement of electron–phonon scattering and energy releasing to the lattice. This process should appear in the lattice temperature curve as a gradual rising edge. Unfortunately, our peak intensity data did not have enough SNR to resolve this effect clearly. Additionally, the tiny change in lattice temperature due to this process weighted too little in the whole electron–phonon coupling such that its influence on TTM fitting is negligible. Therefore, the fitting parameters (t_0 and τ_{e-p}^E) reflected mostly the coupling between the thermalized electrons and lattice, with a delayed t_0 due to the electron thermalization process.

On the other hand, considering the significant electronic thermal stress together with the much better SNR in the determining Bragg peak position, the effect of electron thermalization process is much more clearly revealed in the peak position data. In principle, both non-thermal and thermal electrons could contribute to thermal stress. However, if the contribution from non-thermal electrons is comparable with that of the thermalized ones, we should still see a sharp turning point around the time-zero of the peak position

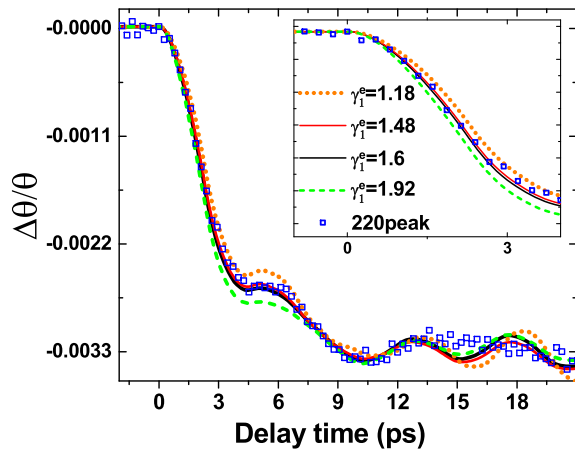


FIG. 4. Fitting the peak position data including the effect of the electron thermalization process. The inset highlights the fittings for the initial 3 ps with different γ_1^e .

change. This, however, was not the case, judged by our peak position data, and it seems such that the electronic thermal stress was also built up gradually. Hence, we assumed that the stress from non-thermal electrons were negligible if compared to that of thermalized electrons. Suppose that the thermalization process of electrons followed an exponential function with a time-constant of τ_{e-e}^E and the lattice contribution to the thermal stress within τ_{e-e}^E was negligible, then Eq. (17) could be modified as

$$\sigma_1(x, t) = \left\{ \begin{array}{l} C_1^l T_{jump} \gamma_1^l (1 - \exp(-\frac{t}{\tau_{e-e}^E}))(1 - \zeta), \\ 0 \leq t < \tau_{e-e}^E \\ C_1^l T_{jump} \gamma_1^l (1 - \exp(-\frac{t}{\tau_{e-e}^E})) \\ \times \left(1 - \zeta \exp\left\{-\frac{t - \tau_{e-e}^E}{\tau_{e-p}^E}\right\}\right), \quad \tau_{e-e}^E \leq t \end{array} \right\}. \quad (20)$$

By replacing Eq. (17) by Eq. (20), the fitting curves matched the data much better, as shown in Fig. 4. In this case, we found that the extracted γ_1^e was still around 1.6.

In summary, we have studied the dynamics of coherent acoustic phonon generation in gold nanofilm induced by fs optical excitation. Under the condition of $\alpha \gg 1$, we were able to disentangle the contribution of the electronic thermal stress to the lattice motion from that of the lattice thermal stress and successfully measured γ^e to be 1.6. We also found that the observed lattice heating through the electron-phonon coupling process started later than the lattice expansion, which could be attributed to the combined effect of electron thermal stress and hot electron thermalization. By taking such a process into account, the fitting was improved, while the extracted γ^e of gold was still around 1.6, consistent with the value of previous studies.

ACKNOWLEDGMENTS

This work was supported by the National Natural Science Foundation of China (Grant No. 11774409), the National Science Foundation (Grant No. DMR-0907262), the National Science

Foundation Cooperative (Agreement No. DMR-1157490), and the State of Florida.

REFERENCES

- P. Ruello and V. Gusev, "Physical mechanisms of coherent acoustic phonons generation by ultrafast laser action," *Ultrasonics* **56**, 21–35 (2015).
- W. S. Fann, R. Storz, H. W. K. Tom, and J. Bokor, "Direct measurement of nonequilibrium electron-energy distributions in subpicosecond laser-heated gold films," *Phys. Rev. Lett.* **68**(18), 2834–2837 (1992).
- R. H. M. Groeneveld, R. Sprik, and Ad. Lagendijk, "Femtosecond spectroscopy of electron-electron and electron-phonon energy relaxation in Ag and Au," *Phys. Rev. B* **51**(17), 11433–11445 (1995).
- N. Del Fatti, C. Voisin, M. Achermann, S. Tzortzakis, D. Christofilos, and F. Vallée, "Nonequilibrium electron dynamics in noble metals," *Phys. Rev. B* **61**(24), 16956–16966 (2000).
- J. Hohlfeld, S. S. Wellershoff, J. Gudde, U. Conrad, V. Jahnke, and E. Matthias, "Electron and lattice dynamics following optical excitation of metals," *Chem. Phys.* **251**, 237–258 (2000).
- G. Tas and H. J. Maris, "Electron diffusion in metals studied by picosecond ultrasonics," *Phys. Rev. B* **49**(21), 15046–15054 (1994).
- M. Perner, S. Gresillon, J. März, G. von Plessen, J. Feldmann, J. Porstendorfer, K.-J. Berg, and G. Berg, "Observation of hot-electron pressure in the vibration dynamics of metal nanoparticles," *Phys. Rev. Lett.* **85**(4), 792–795 (2000).
- J. Wang and C. Guo, "Effect of electron heating on femtosecond laser-induced coherent acoustic phonons in noble metals," *Phys. Rev. B* **75**(18), 184304 (2007).
- O. B. Wright, "Ultrafast nonequilibrium stress generation in gold and silver," *Phys. Rev. B* **49**(14), 9985–9988 (1994).
- X. Wang, S. Nie, J. Li, R. Clinite, M. Wartenbe, M. Martin, W. Liang, and J. Cao, "Electronic grüneisen parameter and thermal expansion in ferromagnetic transition metal," *Appl. Phys. Lett.* **92**(12), 121918 (2008).
- S. Nie, X. Wang, H. Park, R. Clinite, and J. Cao, "Measurement of the electronic grüneisen constant using femtosecond electron diffraction," *Phys. Rev. Lett.* **96**(2), 025901 (2006).
- M. Nicoul, U. Shymanovich, A. Tarasevitch, D. von der Linde, and K. Sokolowski-Tinten, "Picosecond acoustic response of a laser-heated gold-film studied with time-resolved x-ray diffraction," *Appl. Phys. Lett.* **98**, 191902 (2011).
- J. G. Collins, G. K. White, and C. A. Swenson, "The thermal expansion of aluminum below 35 K," *J. Low Temp. Phys.* **10**, 69–77 (1973).
- T. H. K. Barron, J. G. Collins, and G. K. White, "Thermal expansion of solids at low temperatures," *Adv. Phys.* **29**, 609–730 (1980).
- H. Park, X. Wang, S. Nie, R. Clinite, and J. Cao, "Mechanism of coherent acoustic phonon generation under nonequilibrium conditions," *Phys. Rev. B* **72**(10), 100301 (2005).
- K. O. Mclean, C. A. Swenson, and C. R. Case, "Thermal expansion of copper, silver, and gold below 30 K," *J. Low Temp. Phys.* **7**, 77–98 (1972).
- X. Wang, H. Park, S. Nie, and J. Cao, "Femtosecond electron diffraction: Probe and control of ultrafast structural dynamics," *Microsc. Microanal.* **11**, 478 (2005).
- X. Wang and Y. Li, "Ultrafast electron diffraction," *Chin. Phys. B* **27**(7), 076102 (2018).
- D. B. Sirdeshmukh, L. Sirdeshmukh, and K. G. Subhadra, *Micro- and Macro-Properties of Solids* (Springer, 2006).
- P. B. Allen, "Theory of thermal relaxation of electrons in metals," *Phys. Rev. Lett.* **59**(13), 1460–1463 (1987).
- L. Waldecker, R. Bertoni, R. Ernstorfer, and J. Vorberger, "Electron-phonon coupling and energy flow in a simple metal beyond the two-temperature approximation," *Phys. Rev. X* **6**(2), 021003 (2016).
- M. Ligges, I. Rajkovic, P. Zhou, O. Posth, C. Hassel, G. Dumpich, and D. Von Der Linde, "Observation of ultrafast lattice heating using time resolved electron diffraction," *Appl. Phys. Lett.* **94**(10), 101910 (2009).
- J. Li, R. Clinite, X. Wang, and J. Cao, "Simulation of ultrafast heating induced structural dynamics using a one-dimensional spring model," *Phys. Rev. B* **80**, 014304 (2009).
- S. D. Brorson, J. G. Fujimoto, and E. P. Ippen, "Femtosecond electronic heat-transport dynamics in thin gold films," *Phys. Rev. Lett.* **59**(17), 1962–1965 (1987).

²⁵Z. Lin, L. V. Zhigilei, and V. Celli, “Electron-phonon coupling and electron heat capacity of metals under conditions of strong electron-phonon nonequilibrium,” *Phys. Rev. B* **77**(7), 075133 (2008).

²⁶Y. Takahashi and H. Akiyama, “Heat capacity of gold from 80 to 1000 K,” *Thermochim. Acta* **109**(1), 105–109 (1986).

²⁷G. Cordoba and C. R. Brooks, “The heat capacity of gold from 300 to 1200 K: Experimental data and analysis of contributions,” *Phys. Status Solidi A* **6**(2), 581–595 (1971).

²⁸D. R. Lide, *CRC Handbook Chemistry and Physics*, 82nd ed. (Chemical Rubber Company, Roca Raton, 2001–2002).